

Revealing the Partially Coherent Nature of Transport in IGZO

Ying Zhao^{1*}, Michiel J. van Setten¹, Anastasiia Kravtsov¹, Pietro Rinaudo^{1,3}, Harold Dekkers¹,
Jacopo Franco¹, Ben Kaczer¹, Mischa Thesberg², Gerhard Rzepa², Franz Schanovsky²,
Attilio Belmonte¹, Gouri Sankar Kar¹, Adrian Chasin¹

¹imec, Leuven, Belgium

²Global TCAD Solutions (GTS) GmbH, Vienna, Austria

³KU Leuven, Leuven, Belgium

*Email: ying.zhao@imec.com

Abstract

Thin-film transistors based on amorphous oxide semiconductors (AOS) are promising candidates for enabling further DRAM scaling and 3D integration, which are critical for advanced computing. Despite extensive research, the charge transport mechanism in these disordered semiconductors remains poorly understood. In this work, we investigate charge transport in the archetypical AOS material, indium gallium zinc oxide (IGZO), across a range of compositions and temperatures using thin-film transistors and Hall bar structures. Our results show that the electrons involved in transport exhibit partially spatial coherence and non-degenerate conduction. Under these conditions, transport is dominated by electron transfer across insulating gaps between locally coherent regions, rather than by degenerate percolative transport above a mobility edge, or by localized-state hopping, both of which are widely assumed in the literature. While fluctuation-induced tunnelling has previously been invoked to describe low-temperature transport in oxide transistors, we show that such behavior originates from partially coherent electronic states and develop a field-effect-aware fluctuation-induced tunnelling (FEAFIT) framework that explicitly accounts for gate modulation of the tunneling landscape. The FEAFIT model accurately predicts experimental data across all compositions, temperatures, and gate voltages, enabling extraction of fundamental transport parameters. These tunnelling parameters are then correlated with electron coherence dimensions and the degree of energetic disorder obtained from first-principles calculations. Our findings advance the fundamental understanding of charge transport in AOS-based transistors and provide a foundation for further performance improvements.

Introduction

Since the seminal work of Nomura¹, indium gallium zinc oxide (IGZO)-based thin-film transistors (TFTs) have found applications in displays^{2,3}, flexible electronics⁴, ubiquitous RFID tags⁵, quasi-non-volatile DRAM⁶⁻⁸, and other technologies essential for the CMOS 2.0 era⁹. These diverse applications stem from the unique properties of amorphous oxide semiconductors (AOS): low-temperature processing (enabling low-cost flexible and printed electronics as well as BEOL compatibility), excellent deposition uniformity (ensuring electrical consistency for large-area displays), low off-currents (providing long retention times in DRAM cells), and electron mobility comparable to crystalline phases. High on-current AOS-based transistors are expected to play a crucial role in achieving ultra-high-density storage devices^{10,11}. A comprehensive understanding of charge transport in AOS is therefore essential for improving intrinsic mobility and advancing this field.

Remarkably, despite their disordered structure, AOS materials exhibit high electron mobility^{1,6,8}. Unlike amorphous silicon (a-Si)^{12,13} and various organic semiconductors^{14,15}, carrier coherence in AOS is not fully destroyed by atomic disorder, allowing electrons to behave as quasi-free waves within confined regions. For example, amorphous IGZO (a-IGZO) can exhibit Hall-effect mobilities at high carrier concentrations^{10,16–18}. A Hall study on doped IGZO reported temperature-independent Hall carrier concentration (n_{Hall}) alongside thermally activated DC conductivity, suggesting degenerate conduction¹⁶. However, classical Lorentz force considerations for Hall measurements apply only to fully delocalized carriers with well-defined drift velocities, not to localized carriers^{19–21}. In materials with mixed localized and delocalized states, Hall measurements can be misleading, which is overlooked in the previous study¹⁶. Furthermore, some researchers have observed temperature-independent conductivity in IGZO at cryogenic temperatures^{18,22}, which contradicts traditional transport models such as Multiple Trapping and Release (MTR) or Variable Range Hopping (VRH)²³.

To reconcile the measured Hall mobility with the thermally activated conductivity in doped IGZO, Kamiya et al. proposed a spatially varying potential landscape with random barrier heights above a distinct mobility edge^{16,24}. However, this percolation-based model is unsatisfactory because it assumes fully coherent electron transport and neglects the impact of energetic disorder, which leads to loss of coherence and the formation of localized states²⁵. Consequently, it fails to reproduce mobility at low temperatures and cannot accurately describe the Seebeck coefficient^{18,25}. More recently, Nenashev et al.²⁶ and Fishchuk et al.^{27,28} introduced a percolation description based on a random band-edge model that accounts for spatial variations in the mobility edge position²⁹. Yet, this approach still does not capture the observed low-temperature features. Lee et al.³⁰ attempted to combine multiple transport models to fit experimental data across wide gate-voltage and temperature ranges, but this method requires 13 fitting parameters and lacks fundamental physical insight. Beyond percolation models, Wang et al.¹⁸ and Nenashev et al.³¹ proposed field-induced lateral tunnelling to explain temperature-independent conductivity at cryogenic temperatures. While these models can reproduce certain experimental trends, they offer limited ability to extract deeper physical insights or establish direct links between film composition, microstructure, and transport properties.

To uncover the nature of transport in IGZO, we modulate the degree of energetic disorder and examine the coherence of electronic states by varying the material composition. Increasing the indium concentration enhances electron doping efficiency and effective mobility^{1,10,32,33}, whereas higher gallium content introduces greater energetic disorder along the transport paths^{17,25,34}. Our results show that chemical composition significantly influences the temperature dependence of transport. Specifically, we observe a unique temperature-independent field-effect (FE) conductivity at cryogenic temperatures, which disappears as the Ga content increases. Hall measurements combined with first-principles calculations reveal that electrons remain partially coherent within finite regions, the size of which is determined by composition.

The presence of partial electron coherence implies quasi-free transport within these coherent regions, coupled with fluctuation-induced tunnelling between them. Building on this observation, we propose a new transport model that provides a unified and quantitative description of the temperature-dependent conductivity in amorphous IGZO-based transistors. This model remains valid across the entire experimental range of temperature and gate voltage. Furthermore, we extract the incoherence dimensionality for different a-IGZO compositions, and these physical parameters exhibit consistent trends with first-principles predictions. This

agreement reinforces the partially coherent transport picture and validates our proposed model for a-IGZO.

Results

Temperature dependent transport measurements

We use back-gated a-IGZO TFTs, fabricated on 300 mm wafers, for transport studies (Fig. 1a). The optimized a-IGZO deposition by PVD guarantees film thickness uniformity across the wafer (deposited a-IGZO thickness map in Fig. S1b). As previously reported³², the initial threshold voltage (V_{th0}) increases and the field-effect mobility (μ_{FE}) decreases with increasing Ga content, at a fixed In content ($\sim 39\%$), as shown in Fig. 1b. The μ_{FE} also decreases with increasing Ga content, for fixed In-to-Ga ratio as shown in Fig. 1c. In addition, we observe that Ga-rich a-IGZO films have a larger band gap, as shown by the ellipsometry measurements in Fig. 1d. Assuming that the valence band remains constant due to the O_{2p} metal d hybrids¹, we conclude that Ga-rich a-IGZO has a higher E_{CBM} (referred to the vacuum level), revealing that the Ga concentration affects on the conduction states.

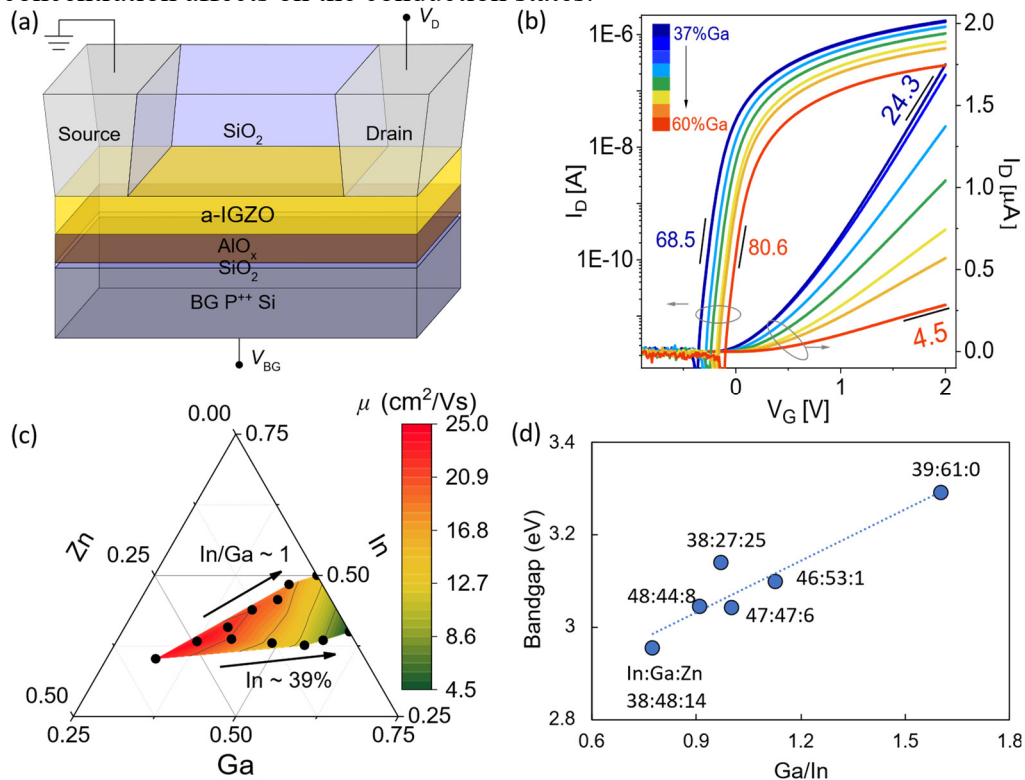


Fig. 1 The fabricated a-IGZO TFTs and composition-related properties. (a) Schematic of back-gated a-IGZO transistor's structure for transport measurement. (b) Transfer characteristics of IGZO TFTs with different compositions under room temperature, at $V_D = 0.05$ V. (c) Ternary composition diagram with colour-mapped field effect mobility (μ_{FE}) under two routes of varying IGZO compositions, fixed In concentration at 39 % and fixed In/Ga ratio at 1. (d) Band gap characterization by ellipsometry for different compositions, the ratio among In, Ga and Zn is marked.

We observe a strong impact of composition on the temperature-dependent conductivity characteristics. Fig. 2a shows the temperature dependence of conductivity at a fixed gate voltage ($V_G - V_{FB}$) of three a-IGZO compositions, Ga37 (In:Ga:Zn = 39:37:24), Ga49 (In:Ga:Zn = 39:49:12) and Ga61 (In:Ga:Zn = 39:61:0). The flat band voltages (V_{FB}) are obtained from TCAD calibration in Note S1. Conductivity is thermally activated for all compositions and the temperature dependence increases with Ga content. We

phenomenologically divide the experimental conductivity into three regions, where the conductivity follows a linear relation with temperature on a log scale. For the first two regimes, all compositions share the same temperature range: the first regime spans 300 K to 120 K, and the second spans 120 K to 50 K. Below 50 K, Ga37 gradually reaches a saturation state with temperature independence, while Ga61 continues to exhibit significant thermal activation down to 10 K. Ga49 exhibits moderate slopes of thermal activation, which saturate at high gate voltage (see Fig. S7). For each composition and regime, we fit an Arrhenius dependence to obtain the activation energy E_a as a function of gate voltage. The extracted E_a 's in the different regimes are shown in Fig. 2b. The E_a of Ga61 is more than twice than the E_a of Ga37 in all regimes. Specifically, in the last regime for $T < 40$ K, $E_{a,3}$ in Ga61 is 10 – 20 meV, whereas in Ga37, $E_{a,3}$ approaches zero. The gradual suppression of the temperature dependence cannot be accounted for by thermally activated MTR or VRH models, indicating a transport regime that becomes largely insensitive to thermal activation and lies beyond classical hopping or trapping descriptions. The finite activation energies ($E_{a,3} > 0$ eV) in Ga49 and Ga61 indicate that, although thermal activation is strongly suppressed, electrons still experience energy disorder along their conducting paths.

Besides the activation energy, the exponent of a power-law dependence between conductivity and the applied $V_G - V_{FB}$ (Fig. S8) can provide more insights into the electron transport disorder according to Vissenberg–Matters model^{35,36}. The value of the exponent γ decreases with temperature but increases with Ga concentration, as depicted in Fig. 2c. However, unlike the linear temperature dependence of γ that identifies a hopping mechanism^{36,37}, in a-IGZO the relationship between γ and $1/T$ cannot be described by a simple linear form. Moreover, the temperature dependence of γ is divided into three regimes, as was also observed previously for conductivity. This suggests again that thermally activated hopping of electrons near the Fermi level (E_F) to the mobility edge, and the hopping between isolated electronic states may not be the dominant transport mechanism in a-IGZO.

Probing energetic disorder via tail states characterization

The energetic disorder below the edge of fully delocalized states (E_{dloc}), giving rise to tail states, is calculated using the V_G and temperature dependence of the FE conductivity^{38,39} (Note S1). The extracted tail density of states (DOS) quantitatively shows that the energy disorder is tuned by Ga concentration. In Fig.2d we observe that the higher the Ga concentration in a-IGZO, the broader width and the lower density of the extracted tail states near E_{dloc} are. We also find that an exponential function $N_{tail}(E) = N_0 \exp(-E/E_0)$ with a single slope E_0 cannot correctly fit the entire experimentally extracted tail states distribution. Instead, two exponential distributions are needed: one with a narrow width ($E_{0,1}$) and high-density ($N_{0,1}$), and another with a broader width ($E_{0,2}$) and low-density ($N_{0,2}$). As the Ga concentration increases from 37% to 61%, $E_{0,1}$ changes from 6 meV to 12 meV and $E_{0,2}$ increases from 50 meV to 157 meV (inset of Fig. 2d). The parameters of the tail states are calibrated by TCAD, confirming the existence of the two tails under E_{dloc} , shown in Note S1.

The two tails of localized states represent different degrees of disorder and contribute to different transport behaviors. The first tail, characterized by a small $E_{0,1}$ and larger $N_{0,1}$, corresponds to localized electron states that are densely distributed near E_{dloc} . These states are dense enough to enable electrons to achieve conduction with an acceptable microscopic conductivity. The first tail is related to the “band edge variation”^{16,25,26}, but in fact the states are globally localized and incoherent. The second deeper tail distribution, with larger $E_{0,2}$ and

smaller $N_{0,2}$, indicates a greater degree of disorder and represents moderate localized electron states.

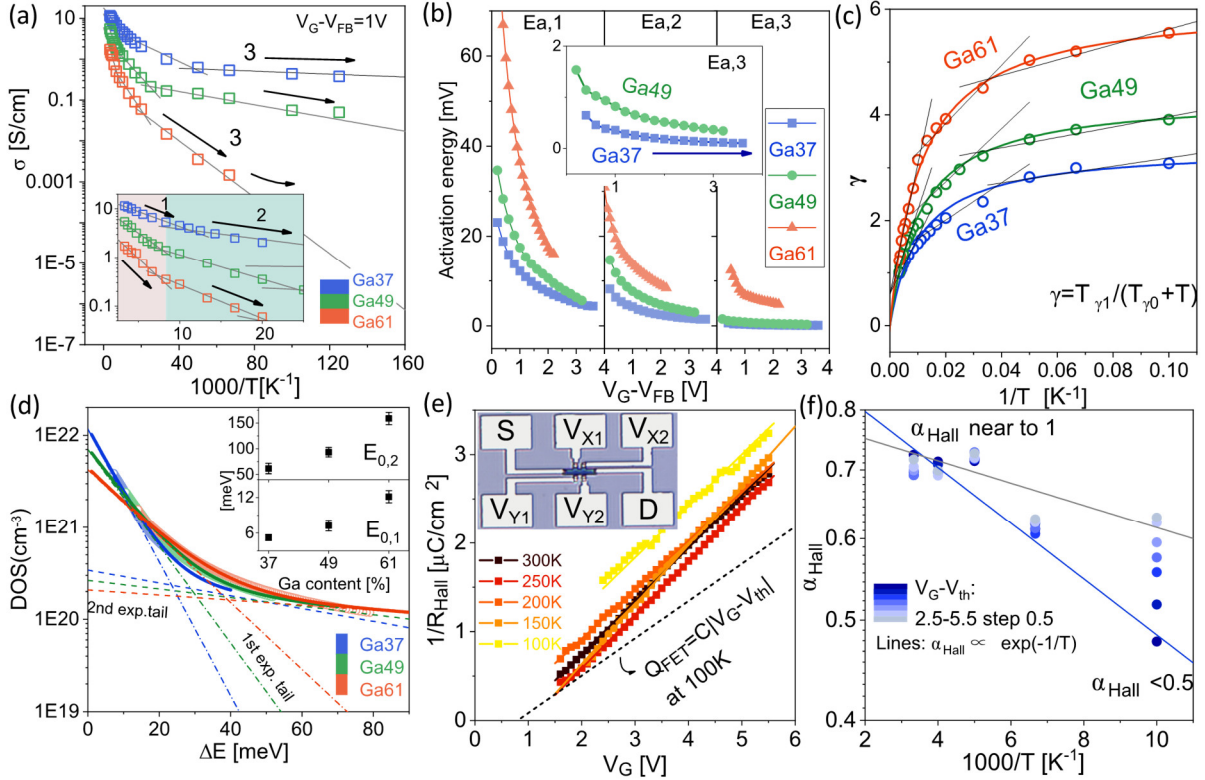


Fig. 2 Unconventional transport behavior in IGZO with varying composition. (a) Temperature dependent conductivity σ in Arrhenius coordinates for three IGZO compositions: Ga37 (In:Ga:Zn = 39:37:24), Ga49 (In:Ga:Zn = 39:49:12) and Ga61 (In:Ga:Zn=39:61:0). σ is divided into three regimes for Arrhenius fitting ($\sigma \propto \exp(-E_{a,(1,2,3)}/k_B T)$, gray lines), labeled as regime 1-3. The inset provides a magnified view from 50 K to 300 K. (b) The extracted E_a of different Arrhenius fitting regimes. (c) Power-law exponent γ extracted from the power-law fits, plotted against inverse temperature ($1/T$) from 10 K to 300 K. The black solid lines indicate linear fits ($\gamma = A_\gamma/T + B_\gamma$) based on VM model³⁵, while the solid-coloured lines correspond to the FEAFIT model fitting ($\gamma = T_{\gamma 1}/(T_{\gamma 0} + T)$). (d) The extracted density of tail states of three compositions. The solid lines represent fittings of two exponential tails. Dash-dot lines correspond to the first exponential tail ($E_{0,1}$, $N_{0,1}$), while dashed lines represent the second tail ($E_{0,2}$, $N_{0,2}$). The insets show the composition dependence of the two tail widths. (e) Temperature dependence of inverse Hall coefficient $1/R_{Hall}$ as a function of V_G . The black dashed lines represent the charge density $Q_{FET} = C_{ox} |V_G - V_{th}|$. The inset shows an optical image of Hall-bar structure used for FE Hall measurement, with a channel width of 6 μm and length of 34 μm . (f) Temperature dependence of carrier coherence factor α_{Hall} under varying $V_G - V_{th}$. The solid lines serve as a thermal activation guide for eye.

Field effect Hall measurements

We now reveal the incoherent nature of transport and corroborate the extracted high density of tail states in a-IGZO by a Hall-effect measurement in field-effect transistors (FETs), which is a more rigorous method^{19,20,40} than a direct Hall measurement in doped IGZO film^{15,16}. AC Hall measurements were performed on the standard composition (Ga37) a-IGZO FETs using the Hall-bar structure shown in the inset of Fig. 2e. The temperature range used is from 300 K to 100 K, and additional measurement details, data analysis and extraction are provided in methods and supplementary notes. The temperature dependence of the inverse Hall coefficient ($1/R_{Hall}$) as a function of V_G is shown in Fig. 2e. We observe the value of $1/R_{Hall}$ is greater than the total electrostatically induced charge density Q_{FET} , which means the Hall carrier density (n_{Hall}) overestimates the total carrier density (n_{FET}). The overestimation of carrier density is due

to the compensation of Hall voltage (V_{Hall}) by incoherent electrons that are pushed by the transverse field V_{Hall} , causing a drift in the opposite direction of the Lorentz force²⁰. The difference becomes greater at lower temperatures, indicating an increase in contribution of incoherent electrons.

The partial coherence is parameterized by the carrier coherence factor α_{Hall} , defined as $n_{\text{FET}}/n_{\text{Hall}}$ ¹⁹. Less coherent carriers lead to an underdeveloped Hall effect with $\alpha_{\text{Hall}} < 1$ ¹⁹. The value of α_{Hall} in our a-IGZO transistors is less than unity from 300 K to 100 K, as shown in Fig. 2f, indicating a “strong hopping contribution” in transport²⁰. At high temperature and gate bias, α_{Hall} is closer to 1 because E_{F} is close to E_{dloc} and electrons have a greater possibility of achieving global degenerate transport. At low biases and temperatures, α_{Hall} is less than 0.5 since fewer coherent electrons are present. The results of our Hall measurements indicate an absence of fully delocalized electrons and metallic conduction in the a-IGZO transistors. The “variable band edge” used in literature to introduce a metal-insulator transition energy range also does not provide a correct picture. The electron transport occurs within partially coherent states, characterized by narrow tail widths and high densities as we extracted in Fig. 2d, moving as “strong hopping” without a well-defined wave vector \mathbf{k} .

First principles computations

To further the understanding of the electron states of the different compositions, we perform first-principles computations within the density functional theory framework. Per composition, five strongly elongated models of about 500 atoms were generated and carefully optimized to investigate the electronic states. The size of these models, approximately 13 nm in the long direction, allows us to resolve the localization of the conduction orbitals in at least one direction⁴¹. As shown in Fig. 3a, conduction localization is evident in all three structural models. However, we observe orbitals with an extension in the range of many atomic sites. The local density of states, shown in Figs. 3b–d, also reveals the locally coherent nature of isolated low-energy regions. The absence of a continuous connection between these regions, for reasonably accessible Fermi levels, prevents global coherence. We observe a broader spatial spread of orbitals around 8 nm for Ga37, two separated orbitals for Ga49, and a single, highly localized state of about 3 nm for Ga61. This trend indicates that increasing Ga content leads to stronger localization of the conduction states, reflecting reduced electron coherence and suppressed spatial delocalization. In contrast, most prior simulations of amorphous IGZO used cubic cells smaller than 2 nm per side, which are insufficient to capture conduction band localization, often leading to the incorrect conclusion of complete delocalization.

In field-effect transistors, E_{F} is shifted by the gate voltage. As E_{F} increases, more of the low-energy pockets are filled and the spread of electron wavepackets becomes larger. The energy height and spacing of the barriers between the coherent regions become lower and smaller, respectively. As the first-principles simulations use a quasi-1D geometry, the extracted barrier heights and widths may not match the absolute values seen in experiments on full 3D systems. In 3D, electrons can find lower barrier paths that are not present in a 1D cut. However, the relative trends across different compositions, such as increasing barrier separation with Ga content, and the underlying partially coherence-limiting picture are expected to hold in both 1D and 3D regimes.

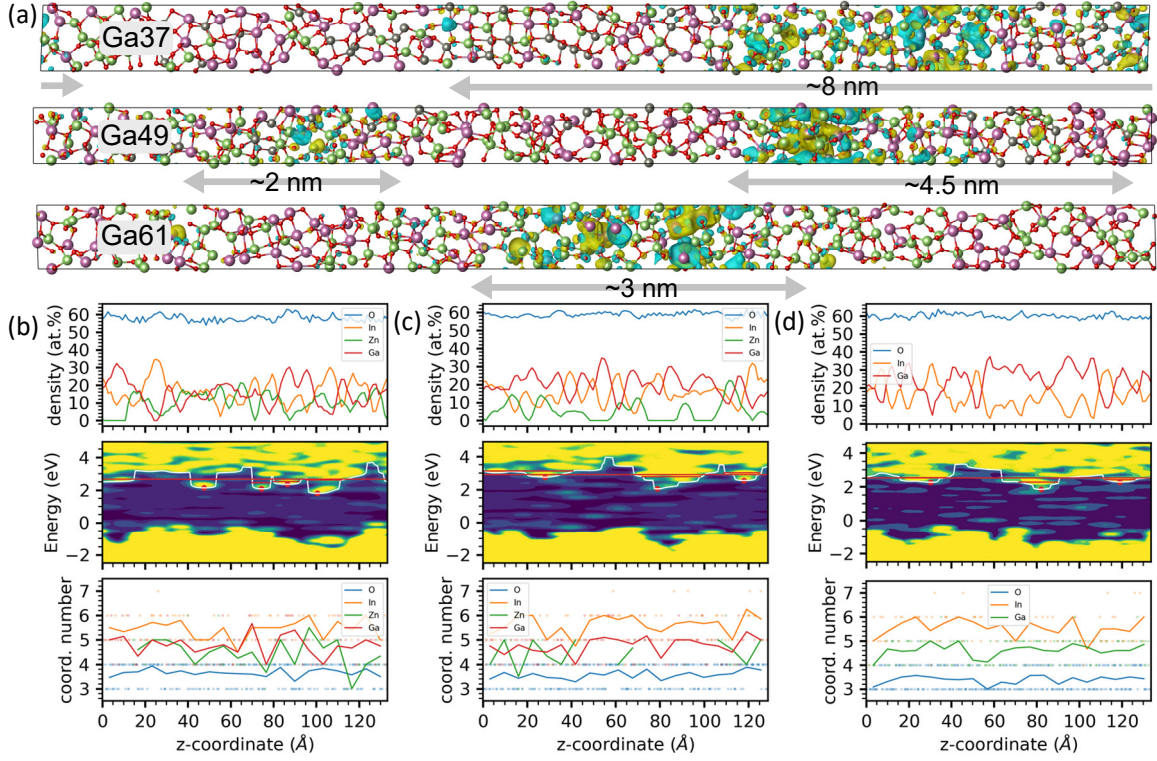


Fig. 3 Electronic structure and structural analysis of three selected models. (a) Examples of conduction orbitals and the atomistic structure, oxygen in red, indium in pink, gallium in green and zinc in grey. (b)-(d) The elemental density, local density of states, and average elemental coordination for the Ga37 (b), Ga49 (c), and Ga61 (d) composition. The local density of states is averaged over the two short dimensions. The white contoured lines are the fixed threshold for tracing the local energy minimum. A direct one-to-one relation with average coordination numbers or with the atomic percentages of the metal species is not distinguishable in this computation.

Energy landscape and electron transport model

The experimental and computational results reveal heterogeneity in the coherence of conduction states in a-IGZO. Electrons remain only locally coherent and cannot achieve fully degenerate metallic conduction over their entire transport path. This means that conventional percolation models, which assume extended coherence above the mobility edge are incorrect. To describe the unconventional transport behavior experimentally, we adopt a different picture of the energy landscape.

The central feature of this landscape is the formation of potential wells. When states below the E_F are occupied, these wells define conducting regions where electrons behave as quasi-free plane waves over a limited range. The gaps between them act as insulating barriers (Fig. 4a). The initial Fermi level E_{F0} , set by composition, doping, metal work function, etc., defines the initial size of conducting and insulating regions. With increasing E_F (e.g. under gate bias), the conducting regions expand and electron wavefunctions spread further. At sufficiently high E_F , wavepackets overlap to form a fully delocalized band where electrons are globally coherent (Fig. 4b). We define the edge of this fully delocalized band as E_{dloc} .

This picture also explains the extracted density of states. Larger conducting regions correspond to smaller energetic disorder, abstracted as a high-density, narrow tail below the band edge. This is followed by a lower-density, broader tail associated with strongly localized states (Fig. 4c). The two-tail profile aligns well with our tail states extractions in Fig. 2d and explains

the strong hopping-like Hall response (Fig. 2e–f). Ga-rich a-IGZO shows broader tails and stronger localization, consistent with higher disorder and smaller conducting regions.

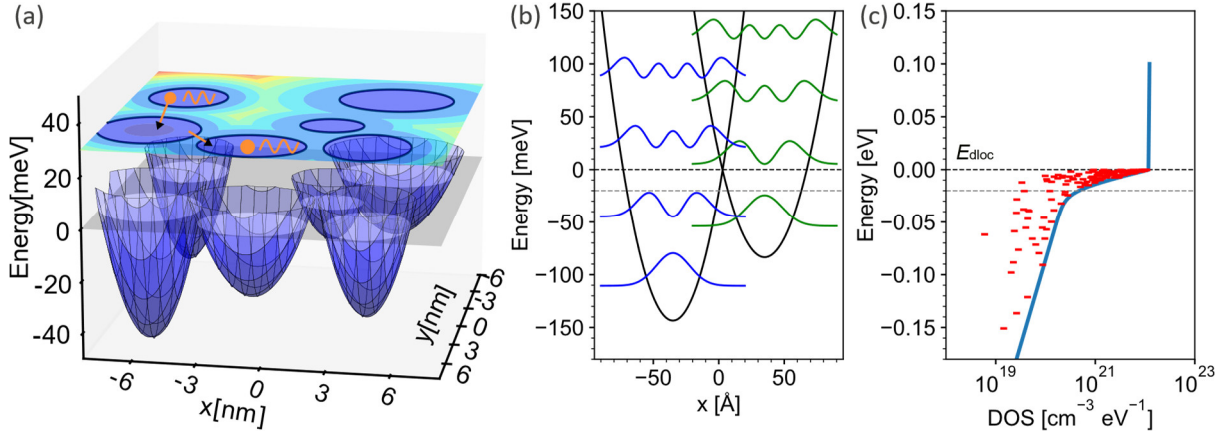


Fig. 4 New potential-well energy landscape. (a) Schematic of the proposed potential-well energy landscape. The gray plane at $E = 0$ eV represents Fermi level. Occupied states (blue regions) consist of conducting regions, outlined by black solid circles in the top-view contour plot. Inside these regions, electrons behave as quasi-free plane waves (orange). In contrast, the surrounding insulating regions form energy barriers that hinder electron transport. (b) The quantized first four wavefunctions ($n = 0, 1, 2, 3$) of electron in two harmonic potential wells. The black dashed line represents the edge of fully delocalized states (E_{dloc}) and gray dashed line marks the transition between different degrees of energetic disorder. (c) Schematic of calculated DOS (blue curve) corresponding to the statistical distribution of electron states in (b). The blue tail DOS is the extracted two exponential tails of Ga37 in Fig. 2d. Red short lines represent localized states in DOS of tail. The gray dashed line marks the transition between two exponential tails.

In such a landscape, we argue that long-range transport is governed by tunnelling between the conducting regions separated by insulating gaps. In a-IGZO, the gaps should be small, because of the high extracted density of tail states and large spread range of electron wavepackets from DFT computations. Each gap can be regarded as a small capacitor (see Fig. 5a), whose capacitance $C_T = \epsilon A/w$, with area A and separated width w . By the equipartition theorem, the mean-square voltage fluctuation across the gap is given by $\langle V_T^2 \rangle = kT/C_T$. Because the capacitance is small for nanoscale junctions, these thermal voltage fluctuations are large and strongly modulate the barrier height and width⁴². Fig. 5b shows that the simulated tunnelling barrier is reduced by the thermally activated voltage fluctuation. We describe this process using a field-effect-aware fluctuation-induced tunnelling (FEAFIT) model. Within this model, the conductivity can be derived as

$$\sigma = \sigma_0 \exp \left[-\frac{T_1(V_G)}{T} S_1(T) - \frac{T_1}{T_0} (V_G) S_0(T) \right], \quad (1)$$

where T_1 sets the activation scale and reflects the characteristic barrier energy linked to disorder, while the ratio T_1/T_0 determines the saturation value in the low-temperature limit, giving the combined effect of barrier height and width on elastic tunnelling. Here $S_1(T) = (\eta^*)^2$, $S_0(T) = \psi(\eta^*)$, with $\eta^*(T)$ the most-probable fluctuation in the thermal averaging. $S_1(T)$ rises from 0 at low temperature to 1 at high temperature, while $S_0(T)$ falls from 1 to 0. Together they describe the smooth crossover from elastic tunnelling to Arrhenius-like activated transport with slope T_1 . This formulation assumes negligible charging energy in the conducting regions, validity of the WKB approximation⁴³, and that detailed barrier shape (image-force corrected rectangular or parabolic) only affects the tunnelling action and is absorbed into the effective parameters T_1 and T_1/T_0 . Note S5 provides explicit description and the derivation of the model.

The influence of the gate field enters naturally through its effect on the tunnelling barrier. At zero gate bias, the tunnelling junction is characterized by an initial barrier height U_0 and width w_0 , both controlled by the position of E_{F0} , which governs the formation of the conducting regions and the insulating gaps between them. As illustrated in Fig. 5c – d, applying a positive gate bias bends the bands downward at the channel surface. This reduces the potential difference between E_{dloc} and the E_F , leading to a smaller effective barrier height $U(V_G)$. At the same time, the spatial extent of occupied potential wells increases, giving a reduced barrier width $w(V_G)$. In the FEAFIT framework, these changes directly map into the transport parameters. A reduction of U decreases the activation scale $T_1(V_G)$, since T_1 reflects the barrier energy. Simultaneous reduction of both U and w decreases the ratio $T_1/T_0(V_G)$ (Eq. S25 and S28 in Supplementary Note S5). Thus, gate bias enhances tunnelling conductivity by lowering the barrier height and narrowing its width, which is captured by the gate dependence of $T_1(V_G)$ and $T_1/T_0(V_G)$ in FEAFIT.

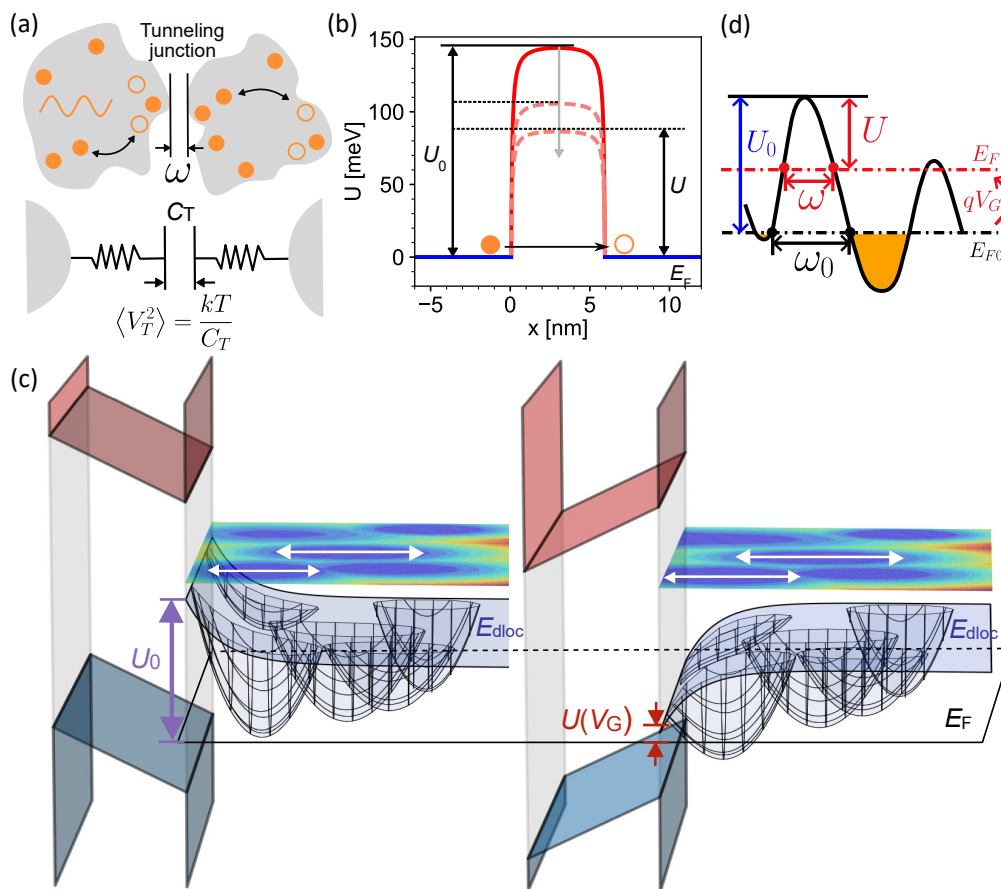


Fig. 5 FEAFIT transport model of a-IGZO. (a) Schematic of tunnel junction between two conducting regions in FEAFIT model. The tunnel junction with width w is modelled as a parallel-plate capacitor C_T . (b) Simulated reduction of the tunnelling barrier due to temperature-induced voltage fluctuations in our model. (c) Band diagram with energy potential wells. Top-view contour plot is cut at E_F . Left: without applied V_G , E_{dloc} bending upward, initial barrier U_0 labelled as purple is higher and conducting regions marked by white arrows are smaller. Right: under positive V_G , E_{dloc} bending downward, enlarging the conducting regions and lowering the barrier height $U(V_G)$. (d) Similar to (c), but with fixed energy profile and a tunable E_F . The downward band bending corresponds to an upward shift in E_F , also reducing the junction width from w_0 to $w(V_G)$.

Model validation and composition-dependent evolution of transport parameters

As shown in Figs. 6a – c, the FEAFIT model reproduces the experimental conductivity of all three a-IGZO compositions over the full temperature range (10 – 300 K) and for different gate

voltages. Without dividing the data into separate regimes, the unified framework accounts for four key features: Arrhenius activation at high temperature, the gradual crossover to temperature-independent behaviour at low-temperature, the suppression of this plateau in Ga-rich compositions, and the overall enhancement of conductivity with increasing V_G .

The extracted transport parameters follow the expected trends. At high temperature the conductivity reduces to $\sigma \propto \exp[-T_1/T]$, where T_1 reflects the barrier energy scale. As Ga concentration increases, the higher energetic disorder leads to larger activation energies (Fig. 2b) and correspondingly larger T_1 values (Fig. 6d). At very low temperature the transport reduces to $\sigma \propto \exp[-T_1/T_0]$, and the ratio T_1/T_0 sets the tunnelling plateau and relates to tunneling barrier width and height. This ratio increases with Ga content, consistent with stronger disorder producing wider and higher barriers (Fig. 6e). In Ga-rich samples, however, this plateau is suppressed. The reduced size of conducting regions and the higher barriers shift the mechanism away from tunnelling, leading to a renewed temperature dependence of conductivity. This behaviour explains the finite value of activation energy in third regime, $E_{a,3}$, and the existent low temperature dependence of σ in Ga49 and Ga61 (Fig. 6a–b). Furthermore, gate bias decreases both T_1 and T_1/T_0 in all compositions, in agreement with the predicted reduction of barrier height and width under positive V_G .

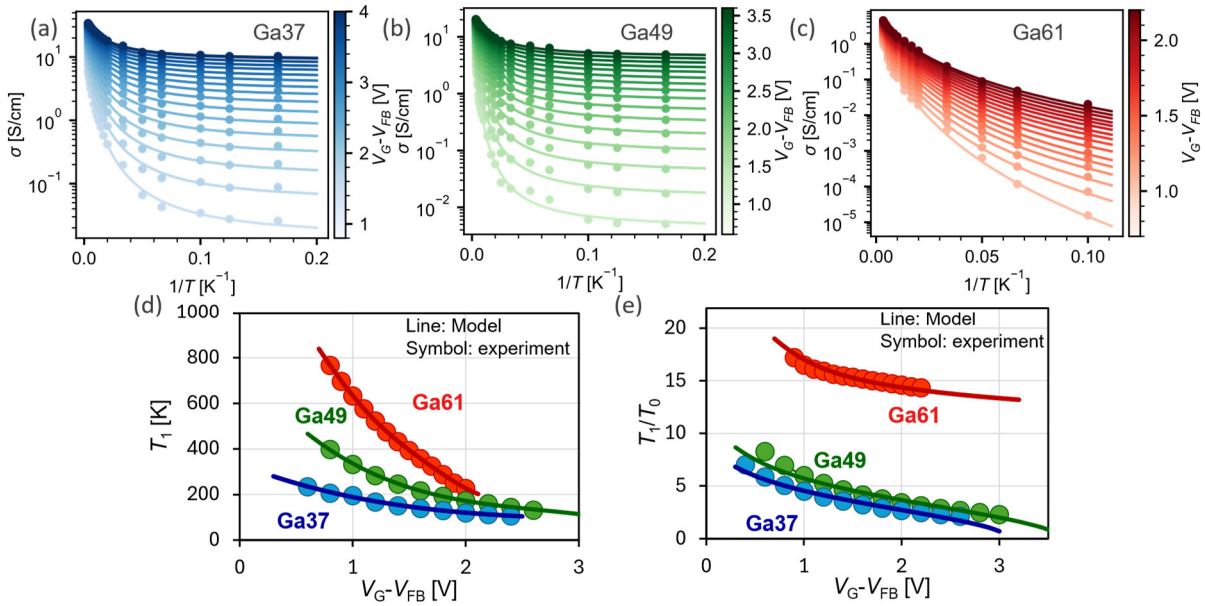


Fig. 6 Model validation and correlation of transport parameters. Comparison between experimentally extracted conductivity ($V_D = 0.05$ V) and the conductivity calculated using the FEAfit transport model for Ga37 (a), Ga49 (b), and Ga61 (c) IGZO. (d–e) The gate bias and composition dependence of model parameters. Symbols represent the experimentally extracted T_1 (d) and T_1/T_0 (e), while solid lines correspond to the values from our transport model, using the physical parameters w_0 and A extracted from fitting.

Beyond reproducing conductivity trends, the model also allows extraction of the initial width w_0 and the effective area A , defined at zero bias. Here, w_0 is the mean separation between conducting regions, and A is the average area of the effective capacitor. Fig. 7a shows that w_0 increases systematically with Ga content, from ~ 4 nm in Ga37 to ~ 8 nm in Ga61, while A rises from $\sim 10^{-16}$ m² to more than 10^{-15} m². In parallel, DFT calculations show that the separation between conduction pockets at the band edge E_{dloc} also increases with Ga content (Fig. 7c), in line with the extracted w_0 from FEAfit.

This agreement between FEAFIT transport fitting and DFT validates the proposed potential-well landscape. More importantly, it shows that the FEAFIT framework is not only able to describe the temperature and gate dependence of conductivity, but also, for the first time, provides barrier parameters with physical meaning. The composition trend is clear: higher Ga content produces larger insulating gaps and higher barriers, corresponding to smaller conducting regions and a Fermi level further from the fully delocalized band edge, which explains the reduced conductivity.

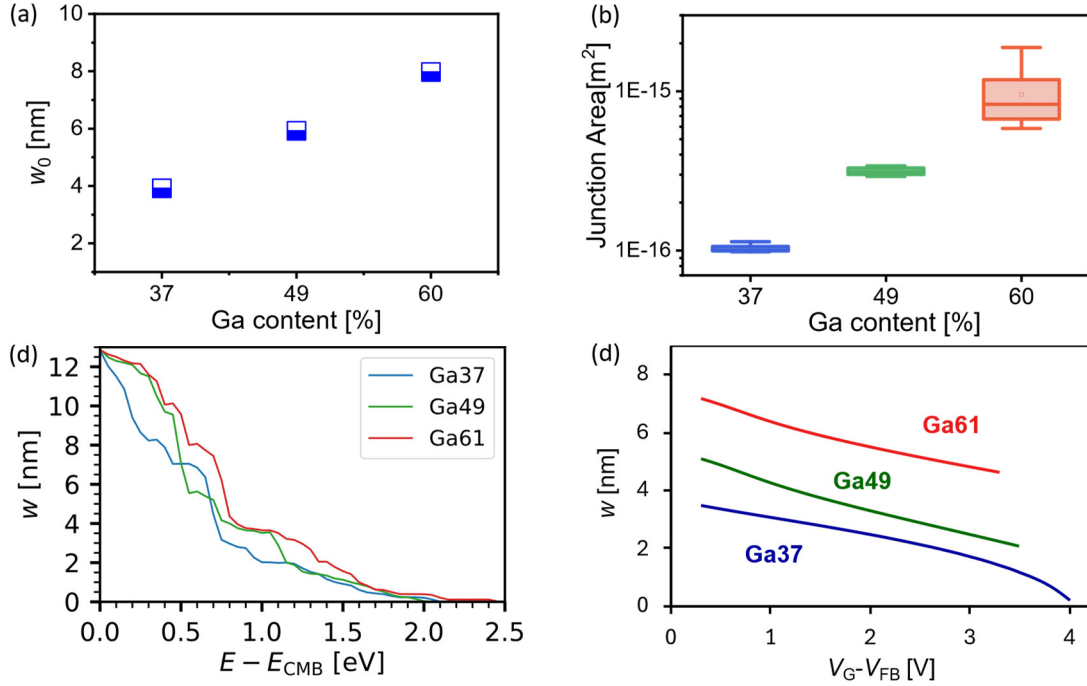


Fig. 7 Tunneling barrier parameters. Composition dependence of initial barrier width w_0 (a) and area A . (b) extracted from FEAFIT. (c) First principles computation results of barrier width w decreasing with larger E_F . E_{CMB} is the absolute minimum of the electron states. The larger the energy separation $E - E_{CMB}$, the closer E_F lies to the fully continuous band edge E_{dloc} . w of Ga-rich IGZO is larger in the energy range that conduction mostly happens. (d) The extracted w of three compositions from FEAFIT decrease with the applied gate voltage.

Discussion

Our proposed view of the Fermi surface morphology and the associated transport mechanism fundamentally differ from both Kamiya's percolation model¹⁶ and classical hopping theories^{23,25}. In Kamiya's framework, electron states are assumed to fill into a continuous Fermi surface, enabling electrons to percolate coherently across the potential landscape, even in the presence of high barriers. In contrast, classical hopping models such as Multiple Trapping and Release (MTR) and Variable Range Hopping (VRH) describe carriers as being confined to individual atomic sites, requiring phonon-assisted jumps to move between them.

Our findings indicate a different scenario: the Fermi level does not extend into the fully delocalized conduction band but remains within a dense tail of states below the edge of fully delocalized states. At high filling levels, these states form finite-size "puddles" of coherent electrons separated by insulating gaps, resembling a dry lake bed picture. These puddles cannot merge into a continuous Fermi surface, preventing global coherence. At lower filling levels (low E_F), conduction becomes even more fragmented, but still not limited to single-site hopping.

Instead, transport is best described as fluctuation-assisted tunnelling between these coherent regions. Rather than invoking percolation at high temperature and hopping at low temperature, the FEAFIT framework provides a unified description based on two key factors: the filling level and the degree of coherence within tail states.

Experimental observations and first-principles calculations strongly support this picture. Temperature-dependent transport measurements in Ga37, Ga49, and Ga61 reveal composition-dependent disorder and tail broadening, while field-effect Hall measurements and DFT pocket analyses confirm the partial coherence of electronic states. The FEAFIT model consistently reproduces conductivity across all temperatures and gate voltages, and even aligns with previously reported data (Fig. S22). Most importantly, it yields barrier dimensionality parameters that agree in both magnitude and composition dependence with DFT predictions. This is the first time such physically meaningful tunneling parameters have been extracted for a-IGZO. Collectively, these results advance the fundamental understanding of charge transport in amorphous oxides and establish a physically grounded framework for material co-design and device performance optimization.

Methods

Different composition a-IGZO wafers fabrication. Back-gated a-IGZO TFTs with gate length and width of 10 μm are used. The devices are processed on a Silicon (p++) substrate. After gate-dielectrics deposition, a 12nm thick a-IGZO films are deposited by co-sputtering three different monoxide targets (InO_x , GaO_x , ZnO_x) in a combinatorial fashion, allowing to tune any a-IGZO composition. A 100 nm PECVD SiO_2 encapsulation layer is deposited. PVD TiN liner and a CVD W filling metals are used for the S/D contacts. Finally, a 350°C O_2 annealing step for 1 hour is applied.

Temperature dependent IV measurement. Temperature-dependent electrical measurements were conducted using a Keithley 2636B sourcemeter in combination with a Lakeshore CPX-LVT cryostat. After dicing the full wafers into small pieces, the samples were mounted in a vacuum chamber pumped to 1e-3 Pa for cryogenic measurement. Wire bonding to a printed circuit board provided stable electrical contacts and minimized additional contact resistance at cryogenic temperatures. Prior to each measurement, thermal equilibrium was ensured by holding the device at the target temperature for 15 minutes. During transport measurements, the drain voltage (V_D) was held at 50 mV, and the common back gate was swept to acquire the transfer IV characteristics.

Ellipsometry measurement. Optical thickness measurements were executed on a-IGZO films with an average thickness range of 24 – 50 nm, deposited on Si using spectroscopic ellipsometry. A KLA SCD100 tool handling 300 mm Si wafers was used with an optical wavelength from 300 – 800 nm. Refractive index and thickness were fitted using the Harmonic Oscillator model. The Tauc Plot method was employed to determine the optical band gap of the film. Here, the attenuation was extracted from the imaginary part of the complex refractive index and its square root is plotted as function of energy⁴⁴. The bandgap is then obtained from the linear fit from 4 eV down to lower values.

Hall measurement. To perform the Hall test, samples ($W \times L = 6 \times 35 \mu\text{m}^2$, fabrication see Note S3) were placed into a Lakeshore CPX-LVT cryostat, pumped to 1e-3 Pa and cooled. The Hall tests were conducted from 100 K to 300 K. In each measurement, magnetic field B was swap

from -2.1 T to 1.5 T in steps of 0.1 T. For electrical measurements, device source was biased at 0 V, drain at 50 mV DC + 5 mV AC (11 Hz), and the gate bias V_G applied through the backside of the sample was swept from -1 to 4 V. Source to drain current I_{XX} was measured, as well as the potential V_{XX} between the two inner pads (#4 and #5), together with Hall voltage V_{Hall} , measured between two transverse pads (#3 and #4). The Hall voltage V_{Hall} was then plotted as a function of magnetic field, linearly fitted, allowing to extract the Hall coefficient $R_H = \frac{I_{XX} \cdot B}{V_{Hall}}$. Details see Note S4.

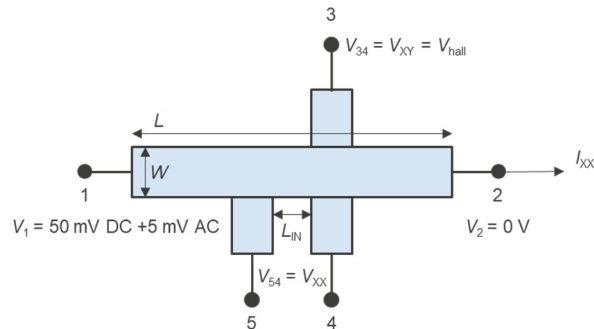


Fig. M1: Biasing schematic for Hall bar structure

DFT. First principles calculations using the density functional theory formalism have been employed using the CP2K software version 2023.2. The hybrid Gaussian and plane wave density functional scheme of CP2K^{45–49} makes the dimensions of the systems needed the required cell dimension computationally feasible. We used the PBEsol generalized gradient approximation for the exchange–correlation functional^{50,51}. The standard double- ζ valence plus polarization (DZVP) basis sets⁵² and pseudo potentials^{53–55} provided with CP2K were used. All calculations were performed using a single \mathbf{k} -point (Γ) to prevent effects caused by the artificial periodicity introduced by the supercell approach from influencing the results. For the structure optimization, we used a maximum geometry change convergence criterion of 5 mBohr and a force convergence criterion of 1 mEH/Bohr. We used a target accuracy for the electronic self-consistency convergence of $1 \times 10^{-6} E_H$. The preparation, execution, monitoring, and postprocessing of all computations reported in this work have been facilitated by our in-house Python package. The amorphous structural models are generated using the decorate-and-relax method proposed by Drabold et al.⁵⁶. In our experience, this approach leads to less defective structures at lower computational costs than melt-and-quench methodologies^{41,57}. The structural optimization, the ‘relax’ part, uses a combination of the Broyden–Fletcher–Goldfarb–Shanno (BFGS) algorithm^{58–61} and time-stamped force-bias MonteCarlo (TFMC)^{62,63}.

Acknowledgement

This work has been enabled in part by the NanoIC pilot line. The acquisition and operation are jointly funded by the Chips Joint Undertaking, through the European Union’s Digital Europe (101183266) and Horizon Europe programs (101183277), as well as by the participating states Belgium (Flanders), France, Germany, Finland, Ireland and Romania. For more information, visit nanoic-project.eu. The first author is deeply grateful to Jiawei Wang for his intellectual guidance during the first author’s doctoral studies, which broadly shaped the first author’s physical understanding of charge transport in IGZO, as well as for introducing the first author to the work of Sheng, which motivated the later consideration of fluctuation-induced tunnelling mechanisms.

Bibliography

1. Nomura, K. *et al.* Room-temperature fabrication of transparent flexible thin-film transistors using amorphous oxide semiconductors. *Nature* **432**, 488–492 (2004).
2. Kamiya, T., Nomura, K. & Hosono, H. Present status of amorphous In–Ga–Zn–O thin-film transistors. *Sci. Technol. Adv. Mater.* **11**, 044305 (2010).
3. Hara, Y. *et al.* IGZO-TFT technology for large-screen 8K display. *J. Soc. Inf. Disp.* **26**, 169–177 (2018).
4. Myny, K. The development of flexible integrated circuits based on thin-film transistors. *Nat. Electron.* **1**, 30–39 (2018).
5. Chasin, A. *et al.* An Integrated a-IGZO UHF Energy Harvester for Passive RFID Tags. *IEEE Trans. Electron Devices* **61**, 3289–3295 (2014).
6. Belmonte, A. *et al.* Capacitor-less, Long-Retention (>400s) DRAM Cell Paving the Way towards Low-Power and High-Density Monolithic 3D DRAM. in *2020 IEEE International Electron Devices Meeting (IEDM)* 28.2.1–28.2.4 (2020). doi:10.1109/IEDM13553.2020.9371900.
7. Duan, X. *et al.* Novel Vertical Channel-All-Around (CAA) In-Ga-Zn-O FET for 2T0C-DRAM With High Density Beyond 4F² by Monolithic Stacking. *IEEE Trans. Electron Devices* **69**, 2196–2202 (2022).
8. Liu, M. *et al.* First Demonstration of Monolithic Three-Dimensional Integration of Ultra-High Density Hybrid IGZO/Si SRAM and IGZO 2T0C DRAM Achieving Record-Low Latency (<10ns), Record-Low Energy (<10fJ) of Data Transfer and Ultra-Long Data Retention (>5000s). in *2024 IEEE Symposium on VLSI Technology and Circuits (VLSI Technology and Circuits)* 1–2 (2024). doi:10.1109/VLSITechnologyandCir46783.2024.10631551.
9. Ryckaert, J. & Samavedam, S. B. The CMOS 2.0 revolution. *Nat. Rev. Electr. Eng.* **1**, 139–140 (2024).
10. Sheng, J. *et al.* Amorphous IGZO TFT with High Mobility of $\sim 70 \text{ cm}^2 / (\text{V s})$ via Vertical Dimension Control Using PEALD. *ACS Appl. Mater. Interfaces* **11**, 40300–40309 (2019).
11. Bai, Z. *et al.* High mobility achieved in InGaZnO TFT with vacuum-gap as insulating layer. *Appl. Phys. Lett.* **121**, 263502 (2022).
12. Geng, D. *et al.* Thin-film transistors for large-area electronics. *Nat. Electron.* **6**, 963–972 (2023).
13. Spear, W. E., Allan, D., Comber, P. L. & Ghaith, A. A new approach to the interpretation of transport results in a-Si. *Philos. Mag. B* **41**, 419–438 (1980).
14. Baranovskii, S. D. Theoretical description of charge transport in disordered organic semiconductors: Charge transport in disordered organic semiconductors. *Phys. Status Solidi B* **251**, 487–525 (2014).
15. Lu, N., Li, L. & Liu, M. A review of carrier thermoelectric-transport theory in organic semiconductors. *Phys. Chem. Chem. Phys.* **18**, 19503–19525 (2016).
16. Kamiya, T., Nomura, K. & Hosono, H. Origin of definite Hall voltage and positive slope in mobility-donor density relation in disordered oxide semiconductors. *Appl. Phys. Lett.* **96**, 122103 (2010).
17. Socratous, J. *et al.* Energy-dependent relaxation time in quaternary amorphous oxide semiconductors probed by gated Hall effect measurements. *Phys. Rev. B* **95**, 045208 (2017).
18. Wang, W. *et al.* Electric field modified Arrhenius description of charge transport in amorphous oxide semiconductor thin film transistors. *Phys. Rev. B* **98**, 245308 (2018).
19. Uemura, T. *et al.* Temperature dependence of the Hall effect in pentacene field-effect transistors: Possibility of charge decoherence induced by molecular fluctuations. *Phys. Rev. B* **85**, 035313 (2012).

20. Yi, H. T., Gartstein, Y. N. & Podzorov, V. Charge carrier coherence and Hall effect in organic semiconductors. *Sci. Rep.* **6**, 23650 (2016).
21. Guo, Z. *et al.* Semimetallization induced Hall anomaly in doped polymers. *Phys. Rev. Res.* **6**, 043180 (2024).
22. Hossain Chowdhury, M. D., Migliorato, P. & Jang, J. Low temperature characteristics in amorphous indium-gallium-zinc-oxide thin-film transistors down to 10 K. *Appl. Phys. Lett.* **103**, 152103 (2013).
23. Mott, N. F. & Davis, E. A. *Electronic Processes in Non-Crystalline Materials*. (Oxford University Press, Oxford, New York, 2012).
24. Kamiya, T., Nomura, K. & Hosono, H. Electronic Structures Above Mobility Edges in Crystalline and Amorphous In-Ga-Zn-O: Percolation Conduction Examined by Analytical Model. *J. Disp. Technol.* **5**, 462–467 (2009).
25. Germs, W. Chr. *et al.* Charge transport in amorphous InGaZnO thin-film transistors. *Phys. Rev. B* **86**, 155319 (2012).
26. Nenashev, A. V. *et al.* Percolation description of charge transport in amorphous oxide semiconductors. *Phys. Rev. B* **100**, 125202 (2019).
27. Fishchuk, I. I. *et al.* Interplay between hopping and band transport in high-mobility disordered semiconductors at large carrier concentrations: The case of the amorphous oxide InGaZnO. *Phys. Rev. B* **93**, 195204 (2016).
28. Fishchuk, I. I. *et al.* Random band-edge model description of thermoelectricity in high-mobility disordered semiconductors: Application to the amorphous oxide In-Ga-Zn-O. *Phys. Rev. B* **105**, 245201 (2022).
29. Welk, A. *et al.* Analysis of Electrical Transport Properties of Amorphous Oxide Semiconductors by an Extended Percolation-Based Random Band-Edge Model. *Phys. Rev. Appl.* **17**, 024007 (2022).
30. Lee, S. *et al.* Trap-limited and percolation conduction mechanisms in amorphous oxide semiconductor thin film transistors. *Appl. Phys. Lett.* **98**, 203508 (2011).
31. Nenashev, A. V. *et al.* Field-enhanced mobility in the multiple-trapping regime. *Phys. Rev. B* **98**, 035201 (2018).
32. Kruv, A. *et al.* The Impact of IGZO Channel Composition on DRAM Transistor Performance. *IEEE Trans. Electron Devices* **70**, 4674–4679 (2023).
33. Hu, K. *et al.* Tri-Layer Heterostructure Channel of a-IGZO/a-ITZO/a-IGZO Toward Enhancement of Transport and Reliability in Amorphous Oxide Semiconductor Thin Film Transistors. *Adv. Electron. Mater.* **11**, 2400266 (2025).
34. Choi, S. *et al.* Excessive Oxygen Peroxide Model-Based Analysis of Positive-Bias-Stress and Negative-Bias-Illumination-Stress Instabilities in Self-Aligned Top-Gate Coplanar In–Ga–Zn–O Thin-Film Transistors. *Adv. Electron. Mater.* **8**, 2101062 (2022).
35. Vissenberg, M. C. J. M. & Matters, M. Theory of the field-effect mobility in amorphous organic transistors. *Phys. Rev. B* **57**, 12964–12967 (1998).
36. Brondijk, J. J. *et al.* Two-Dimensional Charge Transport in Disordered Organic Semiconductors. *Phys. Rev. Lett.* **109**, 056601 (2012).
37. Zhang, Y. *et al.* Probing Carrier Transport and Structure-Property Relationship of Highly Ordered Organic Semiconductors at the Two-Dimensional Limit. *Phys. Rev. Lett.* **116**, 016602 (2016).
38. Lang, D. V., Chi, X., Siegrist, T., Sergent, A. M. & Ramirez, A. P. Amorphouslike Density of Gap States in Single-Crystal Pentacene. *Phys. Rev. Lett.* **93**, 086802 (2004).
39. Kalb, W. L. & Batlogg, B. Calculating the trap density of states in organic field-effect transistors from experiment: A comparison of different methods. *Phys. Rev. B* **81**, 035327 (2010).

40. Wang, S., Ha, M., Manno, M., Daniel Frisbie, C. & Leighton, C. Hopping transport and the Hall effect near the insulator–metal transition in electrochemically gated poly(3-hexylthiophene) transistors. *Nat. Commun.* **3**, 1210 (2012).
41. de Jamblinne de Meux, A., Pourtois, G., Genoe, J. & Heremans, P. Defects in Amorphous Semiconductors: The Case of Amorphous Indium Gallium Zinc Oxide. *Phys. Rev. Appl.* **9**, 054039 (2018).
42. Sheng, P. Fluctuation-induced tunneling conduction in disordered materials. *Phys. Rev. B* **21**, 2180–2195 (1980).
43. Miller, S. C. & Good, R. H. A WKB-Type Approximation to the Schrödinger Equation. *Phys. Rev.* **91**, 174–179 (1953).
44. Klein, J. *et al.* Limitations of the Tauc Plot Method. *Adv. Funct. Mater.* **33**, 2304523 (2023).
45. LIPPERT, B. G. & PARRINELLO, J. H. and M. A hybrid Gaussian and plane wave density functional scheme. *Mol. Phys.* **92**, 477–488 (1997).
46. Frigo, M. & Johnson, S. G. The Design and Implementation of FFTW3. *Proc. IEEE* **93**, 216–231 (2005).
47. VandeVondele, J. *et al.* Quickstep: Fast and accurate density functional calculations using a mixed Gaussian and plane waves approach. *Comput. Phys. Commun.* **167**, 103–128 (2005).
48. Hutter, J., Iannuzzi, M., Schiffmann, F. & VandeVondele, J. cp2k: atomistic simulations of condensed matter systems. *WIREs Comput. Mol. Sci.* **4**, 15–25 (2014).
49. Borštnik, U., VandeVondele, J., Weber, V. & Hutter, J. Sparse matrix multiplication: The distributed block-compressed sparse row library. *Parallel Comput.* **40**, 47–58 (2014).
50. Perdew, J. P., Burke, K. & Ernzerhof, M. Generalized Gradient Approximation Made Simple. *Phys. Rev. Lett.* **77**, 3865–3868 (1996).
51. Perdew, J. P. *et al.* Restoring the Density-Gradient Expansion for Exchange in Solids and Surfaces. *Phys. Rev. Lett.* **100**, 136406 (2008).
52. VandeVondele, J. & Hutter, J. Gaussian basis sets for accurate calculations on molecular systems in gas and condensed phases. *J. Chem. Phys.* **127**, 114105 (2007).
53. Krack, M. Pseudopotentials for H to Kr optimized for gradient-corrected exchange-correlation functionals. *Theor. Chem. Acc.* **114**, 145–152 (2005).
54. Hartwigsen, C., Goedecker, S. & Hutter, J. Relativistic separable dual-space Gaussian pseudopotentials from H to Rn. *Phys. Rev. B* **58**, 3641–3662 (1998).
55. Goedecker, S., Teter, M. & Hutter, J. Separable dual-space Gaussian pseudopotentials. *Phys. Rev. B* **54**, 1703–1710 (1996).
56. Drabold, D. A. Topics in the theory of amorphous materials. *Eur. Phys. J. B* **68**, 1–21 (2009).
57. Setten, M. J. van *et al.* Complex amorphous oxides: property prediction from high throughput DFT and AI for new material search. *Mater. Adv.* **3**, 8413–8427 (2022).
58. BROYDEN, C. G. The Convergence of a Class of Double-rank Minimization Algorithms 1. General Considerations. *IMA J. Appl. Math.* **6**, 76–90 (1970).
59. Fletcher, R. A new approach to variable metric algorithms. *Comput. J.* **13**, 317–322 (1970).
60. Goldfarb, D. A family of variable-metric methods derived by variational means. *Math. Comput.* **24**, 23–26 (1970).
61. Shanno, D. F. Conditioning of quasi-Newton methods for function minimization. *Math. Comput.* **24**, 647–656 (1970).
62. Mees, M. J., Pourtois, G., Neyts, E. C., Thijsse, B. J. & Stesmans, A. Uniform-acceptance force-bias Monte Carlo method with time scale to study solid-state diffusion. *Phys. Rev. B* **85**, 134301 (2012).
63. Neyts, E. C. & Bogaerts, A. Combining molecular dynamics with Monte Carlo simulations: implementations and applications. *Theor. Chem. Acc.* **132**, 1320 (2012).